



Constraints on Metal Oxide and Metal Hydroxide Abundances in the Winds of AGB Stars: Potential Detection of FeO in R Dor

L. Decin^{1,2}, T. Danilovich¹, D. Gobrecht¹, J. M. C. Plane², A. M. S. Richards³, C. A. Gottlieb⁴, and K. L. K. Lee⁴¹ Instituut voor Sterrenkunde, KU Leuven, Celestijnenlaan 200D, B-3001 Leuven, Belgium; leen.decin@kuleuven.be² University of Leeds, School of Chemistry, Leeds LS2 9JT, UK³ JBCA, Department Physics and Astronomy, University of Manchester, Manchester M13 9PL, UK⁴ Harvard-Smithsonian Center for Astrophysics, Cambridge, MA 02138, and School of Engineering & Applied Sciences, Harvard University, Cambridge, MA 02138, USA

Received 2017 December 21; revised 2018 January 25; accepted 2018 January 26; published 2018 March 13

Abstract

Using the Atacama Large Millimeter/submillimeter Array (ALMA), we observed the stellar wind of two oxygen-rich asymptotic giant branch stars, IK Tau and R Dor, between 335 and 362 GHz. One aim was to detect metal oxides and metal hydroxides (AlO, AlOH, FeO, MgO, and MgOH), some of which are thought to be direct precursors of dust nucleation and growth. We report on the potential first detection of FeO ($\nu = 0$, $\Omega = 4$, $J = 11-10$) in R Dor (mass-loss rate $\dot{M} \sim 1 \times 10^{-7} M_{\odot} \text{ yr}^{-1}$). The presence of FeO in IK Tau ($\dot{M} \sim 5 \times 10^{-6} M_{\odot} \text{ yr}^{-1}$) cannot be confirmed, due to a blend with ^{29}SiS , a molecule that is absent in R Dor. The detection of AlO in R Dor and of AlOH in IK Tau was reported earlier by Decin et al. All other metal oxides and hydroxides, as well as MgS, remain undetected. We derive a column density $N(\text{FeO})$ of $1.1 \pm 0.9 \times 10^{15} \text{ cm}^{-2}$ in R Dor, or a fractional abundance $[\text{FeO}/\text{H}] \sim 1.5 \times 10^{-8}$ accounting for non-local thermodynamic equilibrium effects. The derived fractional abundance $[\text{FeO}/\text{H}]$ is a factor ~ 20 larger than conventional gas-phase chemical-kinetic predictions. This discrepancy may be partly accounted for by the role of vibrationally excited OH in oxidizing Fe, or it may be evidence for other currently unrecognized chemical pathways producing FeO. Assuming a constant fractional abundance w.r.t. H_2 , the upper limits for the other metals are $[\text{MgO}/\text{H}_2] < 5.5 \times 10^{-10}$ (R Dor) and $< 7 \times 10^{-11}$ (IK Tau), $[\text{MgOH}/\text{H}_2] < 9 \times 10^{-9}$ (R Dor) and $< 1 \times 10^{-9}$ (IK Tau), $[\text{CaO}/\text{H}_2] < 2.5 \times 10^{-9}$ (R Dor) and $< 1 \times 10^{-10}$ (IK Tau), $[\text{CaOH}/\text{H}_2] < 6.5 \times 10^{-9}$ (R Dor) and $< 9 \times 10^{-10}$ (IK Tau), and $[\text{MgS}/\text{H}_2] < 4.5 \times 10^{-10}$ (R Dor) and $< 6 \times 10^{-11}$ (IK Tau). The retrieved upper-limit abundances for these latter molecules are in accord with the chemical model predictions.

Key words: astrochemistry – circumstellar matter – instrumentation: interferometers – stars: AGB and post-AGB – stars: individual (IK Tau and R Dor) – stars: mass-loss

1. Introduction

The gas-phase elements Ca, Fe, Mg, Si, and Ti are depleted w.r.t. the solar abundances in diffuse clouds. The formation of metal oxides and metal hydroxides and of dust species is suggested as major cause for this depletion. Indeed, a variety of metal oxides and hydroxides are prominent in a wide range of temperature and density environments. The metal oxides TiO, VO, CrO, YO, and ZrO are present in the atmospheres of cool M stars (see, e.g., Scalo & Ross 1976; Castelaz et al. 2000). SiO, TiO, TiO₂, AlO, and AlOH are detected in the winds of oxygen-rich asymptotic giant branch (AGB) stars (e.g., Schöier et al. 2004; Decin et al. 2010, 2018; De Beck et al. 2015, 2017; Kamiński et al. 2016, 2017). Other metal oxides and hydroxides such as CaO, CaOH, FeOH, MgO, and MgOH have been searched in molecular clouds and stars (e.g., Hocking et al. 1979; Kamiński et al. 2013; Sánchez Contreras et al. 2015; Quintana-Lacaci et al. 2016; Velilla Prieto et al. 2017) without success. Laboratory measurements show that FeO can be formed at high temperatures (≥ 1000 K, Cheung et al. 1982) and hence could be abundant in the atmospheres and inner winds of AGB stars. However, until now, FeO has only been detected in interstellar space in

absorption along the line of sight toward the Galactic center H II region Sagittarius B2 Main (Sgr B2 M; Walmsley et al. 2002; Furuya et al. 2003). This detection is interpreted as being due to shocks associated with star formation, which might liberate some fraction of gas-phase elements from the refractory grains. FeO has remained, however, undetected in stellar atmospheres and stellar winds. Here, we report the first potential detection of FeO in the stellar wind of the low mass-loss rate AGB star R Dor (see Section 2). No spectral features of other metal oxides and hydroxides (CaO, CaOH, MgO, and MgOH) and MgS have been seen in the winds of the two oxygen-rich AGB stars R Dor and IK Tau surveyed with ALMA. In Section 3, we show that FeO only accounts for a tiny fraction of the solar iron abundance and derive upper-limit abundances for the undetected metal species. In Section 4, we discuss the derived abundances in the framework of local thermodynamic equilibrium (LTE) and pulsation shock induced non-equilibrium chemistry models for the stellar winds.

2. Observations

We used the Atacama Large Millimeter/submillimeter Array (ALMA) to observe the high mass-loss rate AGB star IK Tau ($\dot{M} \sim 5 \times 10^{-6} M_{\odot} \text{ yr}^{-1}$) and the low mass-loss rate AGB star R Dor ($\dot{M} \sim 1 \times 10^{-7} M_{\odot} \text{ yr}^{-1}$). Data were obtained in 2015 August–September in Band 7 (335–362 GHz) with a spatial resolution of ~ 150 mas (proposal 2013.1.00166.S, PI

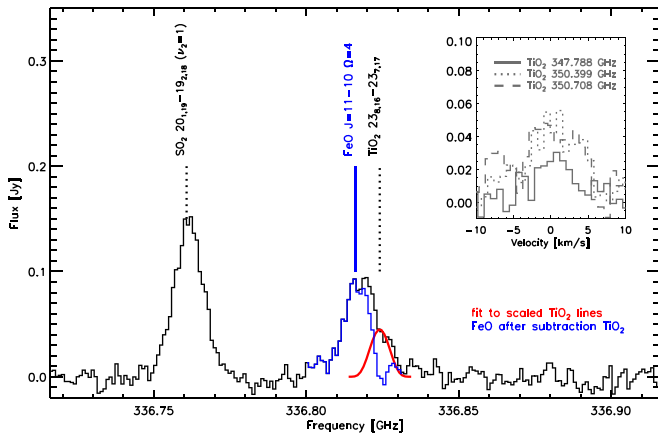


Figure 1. Continuum subtracted ALMA spectrum for R Dor around 336.8 GHz in black extracted for a circular beam with aperture of 300 mas. Two lines of previously identified molecules are observed: SO₂ ($\nu_2 = 1$, 20_{1,19}–19_{2,18}), and TiO₂ (23_{8,16}–23_{7,17}) indicated by the vertical dotted lines in black. The feature at 336.81603 GHz, tentatively identified as the FeO ($\nu = 0$, $\Omega = 4$, $J = 11$ –10) transition, is blended with the line of TiO₂ at 336.82407 GHz. The flux of the TiO₂ line 8 MHz higher in frequency than FeO was estimated by referring to three lines of TiO₂ with similar excitation energies and channel maps that were observed in the same program (see inset in the right-hand side of the panel). From these, a red synthetic profile for the TiO₂ line was derived. Plotted in blue is the observed profile minus the synthetic TiO₂ profile attributed to FeO.

L. Decin). Data reduction was done using the Common Astronomy Software Applications package (CASA; McMullin et al. 2007), and is described in detail in Decin et al. (2018). The spectral restoring beam parameters are in the range of 120–180 mas for IK Tau and 130–180 mas for R Dor. The channel σ_{rms} noise varies between spectral windows, and is in the range of 3–9 mJy for IK Tau and 2.7–5.7 mJy for R Dor. The velocity resolution is 1.6–1.7 km s^{−1} for IK Tau and 0.8–0.9 km s^{−1} for R Dor.

Some 200 spectral features from 15 molecules were identified. Detected species include the gaseous precursors of dust grains such as SiO, AlO, AlOH, TiO, and TiO₂ (Decin et al. 2017, 2018). Sixty-six lines remain unidentified, some of which may belong to OH and H₂O (Decin et al. 2018), or higher excitation rotational transitions that are not included in the current spectral line catalogs of the Jet Propulsion Laboratory (JPL; Pickett et al. 1998) and the Cologne Database for Molecular Spectroscopy (CDMS; Müller et al. 2001, 2005; Endres et al. 2016). The rest frequencies of the unidentified features were carefully compared with the predicted line frequencies of various metal oxides and hydroxides. Rotational transitions of CaO, CaOH, MgO, MgOH (and MgS) do not correspond to any of the unidentified lines.⁵ However, one of the unidentified spectral features in R Dor has a central frequency around 336.815 GHz, with a minor blend at the blue side due to a TiO₂ line at 366.8241 GHz (see Figure 1). We attribute this feature to the FeO ($\nu = 0$, $\Omega = 4$, $J = 11$ –10) transition in the ground electronic $^5\Delta_i$ state with rest frequency $336\,816.030 \pm 0.05$ MHz (Allen et al. 1996). This is the only (potential) FeO line detected in our ALMA data (see also Section 3). We cannot confirm if this FeO transition is present in IK Tau, due to a blend

with the strong ^{29}SiS ($\nu = 1$, $J = 19$ –18) line at 336.815 GHz. However, SiS (and CS) are absent⁶ in R Dor (see Decin et al. 2018), enabling the possibility of detecting and identifying this rotational transition of FeO.

3. Analysis and Results

3.1. The FeO ($\nu = 0$, $\Omega = 4$, $J = 11$ –10) Transition

The ground state of FeO is $^5\Delta_i$ in Hund’s case *a* (Cheung et al. 1981, 1982). As such, there are five spin–orbit components separated by intervals of 190 cm^{−1} (Merer et al. 1982), which are labeled by the quantum number $\Omega = \Lambda + \Sigma$. With Λ and Σ both equal to 2, vector addition gives possible values for Ω between 4 and 0, with the $^5\Delta_4$ component ($\Omega = 4$) lying lowest in energy. The (sub) millimeter wave spectrum of FeO in the $X^5\Delta_i$ state (for $\nu = 0$) has been measured up to 400 GHz in the laboratory by Allen et al. (1996).

The rotational transitions for $J = 11$ –10 of all five Ω components lie in the range of the observed ALMA frequencies (see Table 1 in Allen et al. 1996). Only the $J = 11$ –10 in the lowest energy $\Omega = 4$ component at 336.816030 GHz corresponds to a spectral feature in the ALMA spectrum of R Dor (see Figure 1 and the channel map in Appendix A). The higher excitation Ω components remain undetected. This is unfortunate, as the detection of more than one transition of FeO would strengthen its identification. However, this outcome is not completely unexpected, because transitions between the spin–orbit components are highly forbidden due to the very strong case *a* coupling (Merer et al. 1982), hence they do not support the argument that radiative transitions could cause a significant transfer of population between the Ω -ladders of the $X^5\Delta$ ground state. In this high-density, inner-wind region, collisions might, however, pump the population to the higher energy Ω -levels.

Other rotational transitions in the $\Omega = 4$ spin–orbit component lie outside the observed ALMA frequency range.⁷ The only other transition of FeO hitherto detected in interstellar space belongs to the ($\nu = 0$, $\Omega = 4$) spin–orbit component as well, and it is the lowest ($J = 5$ –4) rotational transition at 153.135 GHz toward the Galactic center H II region Sgr B2 M (Walmsley et al. 2002; Furuya et al. 2003). FeO has been searched for in stellar winds since the early 1980s (Merer et al. 1982) without success. If the spectral feature near 336.815 GHz is indeed caused by FeO (and a minor blend with a TiO₂ line), this would be the first detection of FeO in the wind of an evolved star.

The ALMA data here offer the possibility of estimating the column density of FeO, $N(\text{FeO})$. We therefore need to subtract the contribution of the TiO₂ (23_{8,16}–23_{7,17}) transition, which is slightly blended with the FeO line in the blue wing. We therefore have selected three other TiO₂ transitions with almost equal quantum numbers, excitation energies, line strengths, and channel maps: TiO₂ (24_{2,22}–23_{3,21}) at 347.788 GHz, TiO₂ (26_{0,26}–25_{1,25}) at 350.399 GHz, and TiO₂ (25_{2,24}–24_{1,23}) at 350.708 GHz (see Figure 1). An average flux density of these three lines scaled to the same peak flux was calculated and

⁵ The rotational spectrum of FeOH in the X^6A_1' ground state has not been measured in the laboratory. Detailed quantum-mechanical calculations indicate the dipole moment of 1.368 Debye is favorable, but FeOH is quasi-linear with a small barrier to linearity of less than 300 cm^{−1} and its spectrum may be complex (Hirano et al. 2010).

⁶ It is also possible that the abundance may be too low to detect, even in these sensitive ALMA data.

⁷ Note that in the complete ALMA archive, there are currently no data at high enough sensitivity for another low mass-loss rate AGB star that covers any of the rotational transitions in the FeO $\Omega = 4$ ladder.

fitted using a “soft-parabola” function (see Equation (1) in Decin et al. 2018; see the red line in Figure 1 here) that was then subtracted from the ALMA data. The resulting spectrum (for a circular aperture with beam of 300 mas) is shown in blue in Figure 1. The peak flux of the FeO line is 0.093 Jy and the integrated line flux is $0.79 \text{ Jy km s}^{-1}$. Correcting for a local standard of rest velocity, v_{LSR} , of 7 km s^{-1} (Decin et al. 2018), the half-width of the line at zero intensity, Δv , is 7.5 km s^{-1} . The FeO emission is essentially unresolved with the ALMA beam of $\sim 150 \text{ mas}$ (see the channel map in Figure 6 and discussion in Appendix B), giving us an upper limit for the detected FeO emission of radius $2.5 R_*$.

3.2. FeO Column Density

We use a population diagram analysis to estimate the column density of FeO, $N(\text{FeO})$. Assuming the emission is optically thin, we derive that the column density in the upper ($J = 11$) state, N_u^{thin} , is $1.7 \times 10^{13} \text{ cm}^{-2}$ (see Appendix B). Assuming LTE, $N(\text{FeO})$ can be calculated as

$$N(\text{FeO}) = N_u^{\text{thin}} \frac{Q}{g_u} \frac{1}{\exp(-E_u/kT)}, \quad (1)$$

where g_u is the degeneracy of the upper rotational state, Q is the partition function, and E_u is the energy level of the upper state. The energy of the $J = 11$ rotational level in the $\Omega = 4$ ladder ($E_u = 57.203 \text{ cm}^{-1}$) was calculated with the spectroscopic constants in Allen et al. (1996). For a constant excitation temperature, T_x , the partition function for a linear diatomic molecule is given by (Tielens 2010)

$$Q(T_x) = \sum_i g_i \exp(-E_i/kT_x) \simeq \frac{kT_x}{hB}, \quad (2)$$

where B is the rotational constant of FeO in units of Hz; $B = 15493.63255 \text{ MHz}$ (Allen et al. 1996).

A first estimate on the excitation temperature, T_x , can be obtained from calculating the (upper limit) of the cross-ladder temperature using the fact that the FeO ($v = 0$, $\Omega = 3$, $J = 11-10$) at 338.844 GHz is undetected in our survey. For an energy difference between the Ω -ladders of 190 cm^{-1} (Merer et al. 1982) and a σ_{rms} of 4 mJy (hence $3\sigma_{\text{rms}}$ of 12 mJy), we derive that the cross-ladder temperature, T_x^{CL} , is $< 130 \text{ K}$. If the cross-ladder populations were controlled by collisions, T_x^{CL} would be a direct measure of the kinetic temperature, T_{kin} , provided cross-ladder radiative transitions are negligible, and a lower limit if not (Thaddeus et al. 1984). The estimated kinetic temperature in the region between 1 and $2.5 R_*$ ranges between 1300 and 2400 K (Decin et al. 2017). As cross-ladder transitions are only weakly permitted (see Section 3.1), the cross-ladder temperature is expected to be higher than the temperature within the ladders, because populations (within a ladder) rapidly decay by emission of millimeter-wave photons (Thaddeus et al. 1984). Because other rotational transitions in the $\Omega = 4$ ladder are not in the frequency window of the ALMA data, we cannot calculate the excitation temperature within a ladder. Thaddeus et al. (1984) were able to derive the “within” and “cross”-ladder temperature for the $X^1 A_1$ SiCC molecule—whose $\Delta K_a = 2$ electric dipole transition moments are small—in the carbon-rich AGB star CW Leo, being 10 K and 140 K , respectively. Using a lower limit of 10 K for the excitation temperature of FeO seems unreasonably low, as FeO is detected in the inner wind of

R Dor ($r \leq 2.5 R_*$) in contrast to detection of SiCC in the outer wind of CW Leo. We henceforth assume a lower limit for the excitation temperature of 80 K . Assuming that the excitation temperature can be as high as 2000 K , the derived column density of FeO, $N(\text{FeO})$ varies between 2×10^{14} and $2 \times 10^{15} \text{ cm}^{-2}$, or $N(\text{FeO})$ is $1.1 \pm 0.9 \times 10^{15} \text{ cm}^{-2}$.

Using the equation of mass conservation $\dot{M} = 4 \pi r^2 \rho(r) v(r)$, where $\rho(r)$ is the gas density and $v(r)$ is the gas velocity, one can calculate the H_2 density, $n(\text{H}_2)$, assuming all hydrogen to be locked in H_2 . The H_2 column density, $N(\text{H}_2)$, is dependent on the gas velocity $v(r)$. As shown by Decin et al. (2018), our knowledge of the gas velocity in the inner wind of R Dor is limited. Using the velocity β -laws described by Decin et al. (2018) (their Equations (2)–(4)), we derive that $N(\text{H}_2)$ is $\sim 2 \times 10^{22} \text{ cm}^{-2}$ for a column with length between 1 and $2.5 R_*$. Hence, the ratio $N(\text{FeO})/N(\text{H}_2)$ is estimated to be $\sim 5.5 \pm 4.5 \times 10^{-8}$.

The FeO level populations might, however, violate the assumption of a Boltzmann distribution. There are strong transitions between the ground $X^5 \Delta$ electronic state of FeO to the $^5 \Pi$ and $^5 \Phi$ excited electronic states near $10,000 \text{ cm}^{-1}$ (Cheung et al. 1982), and owing to the large spin-orbit coupling between these three states, the $X^5 \Delta$ state has some excited state character that may enhance $\Delta \Omega \pm 1$ transitions between spin-components. Also, rotational levels within one Ω ladder might be subject to radiative excitation effects. To check for the impact of the latter, we have calculated the frequencies, upper state energies, and Einstein-A coefficients for the rotational transitions in the ($v = 0$, $\Omega = 4$) spin component (see Appendix C). This allows us to calculate $[\text{FeO}/\text{H}_2]$ by solving the statistical equilibrium equations (see Section 3.3).

3.3. Derivation of the (Upper Limit) Abundance of FeO, MgO, MgOH, CaO, CaOH, and MgS

To derive the abundance of FeO and the upper-limit abundance of the undetected species, we use the same procedure as for the determination of the AlO, AlOH, and AlCl abundances in R Dor and IK Tau outlined in Decin et al. (2017). In short, we modeled the ALMA data using a non-LTE radiative transfer model based on the Accelerated Lambda Iteration method (Maercker et al. 2008), which allows us to derive the global mean molecular density assuming a 1D geometry. The gas kinetic temperature and velocity have been approximated by a power-law distribution. The gas density, $\rho(r)$, is calculated from the equation of mass conservation. The fractional abundance of the Al-species w.r.t. H_2 was assumed either to be constant up to a certain maximum radius, R_{max} , or to decline according to a Gaussian profile centered on the star for both targets $f(r) = f_0 \exp(-(r/R_e)^2)$, with f_0 the initial abundance and R_e the e -folding radius.

Collisional excitation rates have not been published for these six molecules (as was the case for AlO, AlOH, and AlCl). Hence, we have used the values from other molecules as substitutes, scaling for the difference in molecular weight. The HCN- H_2 system (Green & Thaddeus 1974) was used to extract the collisional rates for MgOH, CaOH (and AlOH), and the SiO- H_2 system (Dayou & Balança 2006) for FeO, CaO, MgO, MgS (and AlO, AlCl). The collisional rates are used in the form that appears in the LAMDA database⁸ (Schöier et al. 2005). Einstein-A coefficients were calculated from the

⁸ <http://home.strw.leidenuniv.nl/~moldata/>

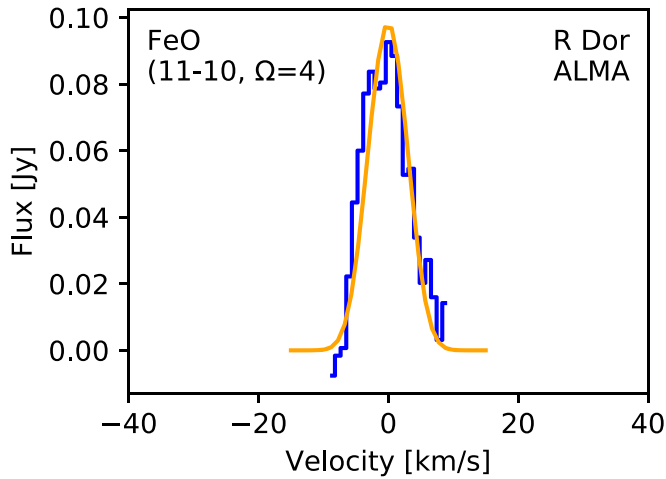


Figure 2. Comparison between the blue extracted ALMA FeO ($v = 0$, $\Omega = 4$, $J = 11-10$) spectrum (corrected for the TiO_2 contribution) and the orange predicted line profile for $[\text{FeO}/\text{H}_2] = 1.4 \times 10^{-8}$, $R_{\text{max}} = 6 R_*$, and $v_{\text{turb}} = 3 \text{ km s}^{-1}$.

quantum-mechanical line strength, S , as given in CDMS (MgOH, CaOH, and CaO), JPL (MgS, MgO), or Appendix C (FeO).

The ALMA R Dor FeO channel map does not allow us to properly deconvolve the ALMA beam (see Appendix B). Assuming the ALMA emission to be essentially unresolved leads to a maximum extent of 150 mas in diameter (or $2.5 R_*$ in radius). Using the moment-0 maps would lead to a larger FeO source size with radius $\sim 6 R_*$. Setting R_e to $2.5 R_*$ (by analogy with AlCl; Decin et al. 2017) and R_{max} to $6 R_*$, the fractional abundance of FeO can be derived. However, for a turbulent velocity, v_{turb} , of 1 km s^{-1} (Decin et al. 2017), the predicted FeO line profile is smaller than observed. As described by Decin et al. (2018), our understanding of the gas velocity in the inner-wind region is limited. Pulsation-induced shocks might result in a radial velocity amplitude of a few km s^{-1} (Nowotny et al. 2010). Allowing the turbulent velocity to be 3 km s^{-1} permits the predicted line profile to reach the observed Δv of 7.5 km s^{-1} (see Figure 2). Using these parameters for the undetected species, the (upper-limit) abundance of the metal species is derived (see Table 1). As for IK Tau, all metal species remain undetected; the upper-limit abundances were only calculated for a constant abundance profile with $v_{\text{turb}} = 1 \text{ km s}^{-1}$ and $R_{\text{max}} = 40 R_*$ (as determined from AlOH and AlCl, Decin et al. 2017).

A principal uncertainty in the abundance calculations concerns the unknown collisional rates. Changing the collisional rates by one order of magnitude only alters the retrieved abundances by 10% or less. The only exception is a lowering by 60% of the calculated FeO abundance if the collisional rates were a factor 10 lower.

4. Discussion

Both the LTE and non-LTE approach render a similar abundance $[\text{FeO}/\text{H}_2] \sim 3 \times 10^{-8}$ in the inner wind of R Dor; or $[\text{FeO}/\text{H}] \sim 1.5 \times 10^{-8}$ assuming all hydrogen to be locked in H_2 for the radiative transfer calculations. In this section, we compare this derived abundance with chemical equilibrium and chemical-kinetic network model predictions (cf. earlier work done by, e.g., Cherchneff 2006; Gail & Sedlmayr 2013; Gobrecht et al. 2016).

Table 1
Derived Abundances for the Metal Species in R Dor and IK Tau

Molecule	R Dor		IK Tau
	Constant f for $R_{\text{max}} = 6 R_*$	f_0 for $R_e = 2.5 R_*$	Constant f for $R_{\text{max}} = 40 R_*$
$[\text{FeO}/\text{H}_2]$	1.4×10^{-8}	5×10^{-8}	$< 6.5 \times 10^{-10}$
$[\text{MgO}/\text{H}_2]$	$< 5.5 \times 10^{-10}$	$< 4 \times 10^{-9}$	$< 7 \times 10^{-11}$
$[\text{MgOH}/\text{H}_2]$	$< 9 \times 10^{-9}$	$< 4.5 \times 10^{-8}$	$< 1 \times 10^{-9}$
$[\text{CaO}/\text{H}_2]$	$< 2.5 \times 10^{-9}$	$< 1.7 \times 10^{-8}$	$< 1 \times 10^{-10}$
$[\text{CaOH}/\text{H}_2]$	$< 6.5 \times 10^{-9}$	$< 3.5 \times 10^{-8}$	$< 9 \times 10^{-10}$
$[\text{MgS}/\text{H}_2]$	$< 4.5 \times 10^{-10}$	$< 2.3 \times 10^{-9}$	$< 6 \times 10^{-11}$

4.1. Description of Gas-phase Chemical Kinetics Models

The gas-phase network used in this study contains seven atomic (H, He, C, O, Ca, Mg, and Fe) and 15 molecular (H_2 , H_2O , O_2 , OH, CO, CO_2 , CaO, CaOH, CaH, MgO, MgOH, MgH, FeO, FeOH, and FeH) species that take part in 59 reactions. The elemental abundances are retrieved from the FRUITY stellar evolution database (Cristallo et al. 2015); dust formation is not accounted for, as we focus on the region where the bulk of the dust has not yet formed.

The gas-phase reaction rate coefficients are taken from the literature where available and extrapolated to the high temperatures of an outflow using transition state theory (TST; Atkins 1998) with molecular constants (vibrational frequencies, rotational constants) calculated using quantum theory. The rate coefficients for reverse reactions were then calculated assuming detailed balance. The list of all chemical reactions involved is given in Table 3 in Appendix D.

The oxides of Ca, Fe, and Mg are produced by reactions with O_2 , CO_2 , H_2O , and OH releasing O, CO, H_2 , and H, respectively, and the hydroxides of Ca, Fe, and Mg are formed by reactions with H_2O and OH. Moreover, the metal oxides (CaO, FeO, and MgO) are linked to the hydroxides by reaction with molecular hydrogen H_2 . Generally, small (reduced) networks might introduce oversimplifications compared with extensive, complete reaction networks. However, the metallic Ca–Mg–Fe chemistry is largely decoupled from the remaining gas-phase chemical families (e.g., sulfur, nitrogen, silicon). We also compared the modeled OH (and H_2O) abundance with the study of Gobrecht et al. (2016), who used an extensive chemical network with 100 species and 424 reactions (including the N, S, and Si chemistry). We find similar trends and absolute values of the OH abundance in both models. The reactions R7, R8, and R11–R16 have the largest impact on the OH chemistry and determine the H_2O –OH balance. In addition, the abundances of the prevalent species CO, CO_2 , H_2O , and OH agree with observations.

The physical conditions experienced by the upper atmosphere of R Dor are described by a parcel of gas that is initially at rest at the photosphere and is in thermodynamic (thermal, chemical, radiative, and mechanical) equilibrium. We assume that the stellar pulsation, originating from the interior of the star, has steepened in a shock and hits the gas parcel. As a consequence, gas in the cube is compressed, heated, and accelerated outward. The temperature and density profiles are calculated following Bertschinger & Chevalier (1985) for a 10 km s^{-1} shock and a diatomic gas with pre-shock conditions of $T_0 = 2400 \text{ K}$ and $n_0 = 1 \times 10^{14} \text{ cm}^{-3}$ (see, e.g., Figure 10 in Freytag et al. 2017). Hydrodynamic calculations

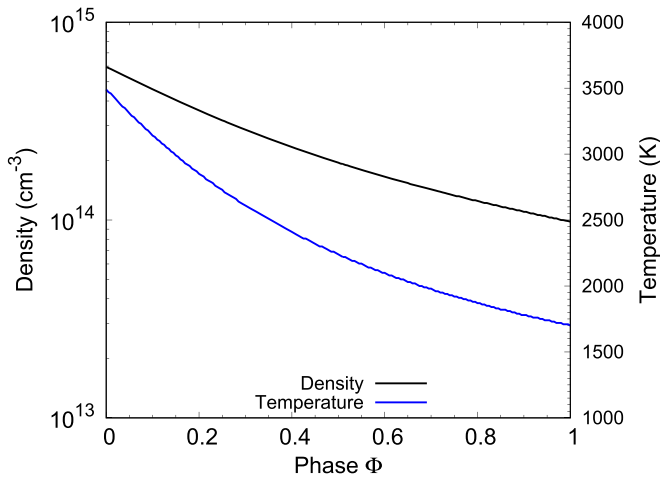


Figure 3. Gas temperature and number density variation in the post-shock gas over one pulsation period at $1 R_*$.

(Nowotny et al. 2010) have shown that the amplitude of the velocity variation, hence the shock velocity is slightly larger than the terminal wind velocity (being $\sim 5.5 \text{ km s}^{-1}$; see discussion in Decin et al. 2018). At the shock front, gas temperature and density take peak values of $T = 3500 \text{ K}$ and $n = 6 \times 10^{14} \text{ cm}^{-3}$, respectively, and subsequently decrease with an exponential decay in the post-shock gas (see Figure 3). We ran the gas-phase chemistry model over a full pulsation period (332 days; Bedding et al. 1998), and followed the change in the atomic and molecular abundance profiles over one pulsation phase (with the phase defined as the decimal part of $(t-T_0)/P$, with T_0 the epoch of the start of the pulsation cycle and P the period); see Figure 4. We note that the abundance variations within a pulsation period are much larger than the cycle-to-cycle variations in the periodic pulsation model.

To probe the accuracy of the chemical kinetics code and reaction network, we performed runs at constant temperature ($T = 2400 \text{ K}$) and density ($1 \times 10^{14} \text{ cm}^{-3}$), and compared the results with equilibrium abundances with the same conditions. For the large majority of molecules, the differences are small and within a factor of two. Exceptions are O_2 , FeOH , MgO , and MgOH , which differ by factors of up to 6–9. We conclude that our small network describes the chemical behavior in the inner wind of R Dor with sufficient accuracy. The relatively small differences between equilibrium and chemical-kinetic abundances may arise from the incomplete network or from an insufficient characterization of some molecules (FeOH , MgOH) and their related reaction rate coefficients.

4.2. Outcome of the Gas-phase Chemical Kinetics Models

The predicted abundances for the metal oxides and metal hydroxides are shown in Figure 4. In the immediate post-shock region (pulsation phase, ϕ , 0.0–0.2), the dissociated molecules start to reform and reach peak abundances between 1.1×10^{-12} ($[\text{MgO}/\text{H}]$) and 7.4×10^{-10} ($[\text{FeO}/\text{H}]$) in the cooling post-shock gas ($\phi = 0.2$ –1.0). While the upper-limit abundances for the undetected species in R Dor (Table 1) are in accord with the model results, the predicted FeO abundance is a factor 20 lower than derived from the ALMA data. The main processes leading to the formation of FeO are $\text{Fe}+\text{OH}$ (R42 in Table 3) and $\text{Fe}+\text{H}_2\text{O}$ (R58). The first reaction dominates at early phases $\phi < 0.5$, whereas the latter is only important at

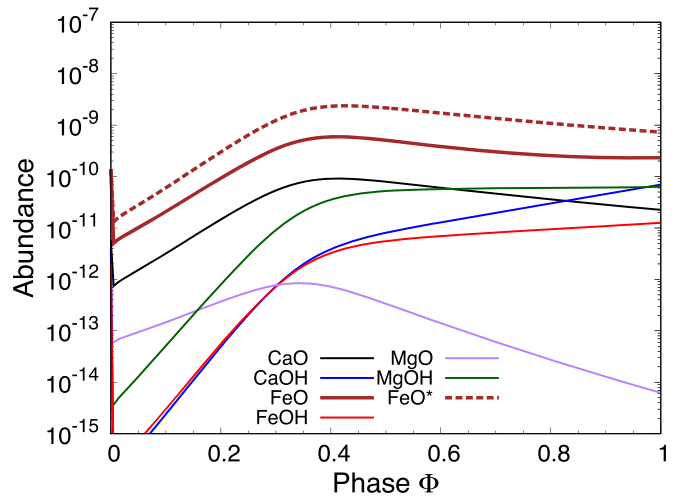


Figure 4. Predicted abundances for the metal oxides and hydroxides with respect to the total gas number density as a function of pulsation phase ϕ at $1 R_*$. FeO^* corresponds to the model abundance, including vibrationally excited OH molecules.

later phases $\phi > 0.5$. The main FeO destruction channel is the reaction $\text{FeO}+\text{H} \rightarrow \text{Fe}+\text{OH}$ (R43).

Provided the FeO identification is correct, a number of suggestions can be used to explain the discrepancy between observed and predicted FeO abundance. It might be that the chemical network is not complete or that the use of detailed balance to estimate some of the rate coefficients is not correct in this environment where molecular vibrational models may not be thermally equilibrated. Another possibility is the sputtering of dust grains, although this seems unlikely since the grains close to the star should be Fe-free silicates or alumina (Khouri et al. 2016) and sputtering products such as O will actually decrease FeO (R39). Although fresh molecular O_2 might react with Fe, which is abundantly present (3.1×10^{-5} relative to H), R38 has a very large activation energy (see Table 3). We here propose an alternative scenario, following the idea of Elitzur et al. (1976), that the $\text{Fe}+\text{OH}$ reaction (R42) might occur from vibrationally excited OH, where R42 would no longer be endothermic. We account for this possibility by reducing the activation barrier of R42 to zero. As a result, the FeO fractional abundance increases by a factor ~ 4 (see the dashed brown line in Figure 4, denoted as FeO^*).

The fraction of vibrationally excited OH in the inner wind of R Dor is, however, unknown. A first-order estimate could come from the assumption of a Boltzmann distribution of states, but this would not represent vibrational disequilibrium. The impact of the amount of vibrationally excited OH can be gauged by reducing the activation barrier, E_a , in reaction (R42) stepwise from 3348 K to 0 K, the latter situation assuming all OH is vibrationally excited hence representing an upper limit (see Figure 5). As expected, the $[\text{FeO}/\text{H}]$ maximum increases, and the maximum value reached is 2.96×10^{-9} for $E_a/R = 0\text{K}$ (see the dashed brown line in Figure 4 and full brown line in Figure 5), which is a factor ~ 5 lower than observed. Accounting for the uncertainties of the thermodynamics properties of the inner-wind region, we conclude that this may be a viable route for the formation of gaseous FeO . However, the results also showcase that using the best available chemical kinetics, FeO is hard to make at the level tentatively observed and presents an important challenge for future chemical models.

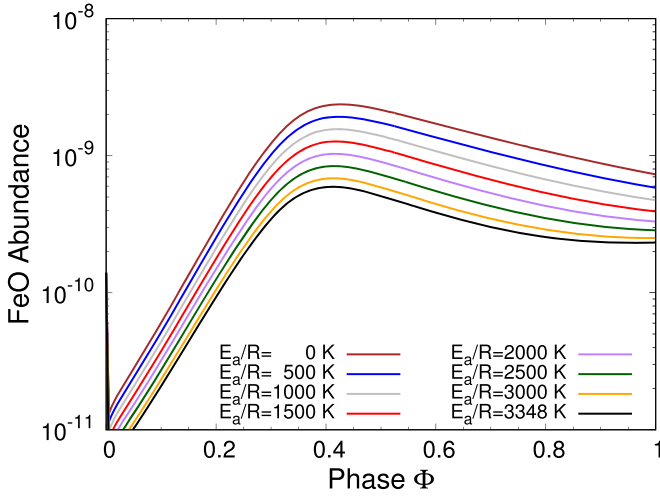


Figure 5. Predicted FeO abundances with respect to the total gas number density as a function of pulsation phase ϕ at $1 R_*$ for different values of the activation barrier, E_a/R , in reaction R42.

We acknowledge A. Merer for the enlightening discussions concerning the FeO structure and B. Drouin for advice on predicting the rotational spectrum. L.D., T.D., D.G., and J.M.C.P. acknowledge support from the ERC consolidator grant 646758 AEROSOL, T.D. acknowledges support from the Fund of Scientific Research Flanders (FWO), J.M.C.P. from the UK Science and Technology Facilities Council (ST/P00041X/1), and C.A.G. and K.L.K.L. from NSF grant AST-1615847. This paper uses the ALMA data ADS/JAO.ALMA2013.1.00166.S. ALMA is a partnership of ESO (representing its member states), NSF (USA) and NINS (Japan), together with NRC (Canada) and NSC and ASIAA (Taiwan), in cooperation with the Republic of Chile. The Joint ALMA Observatory is operated by ESO, AUI/NRAO and NAOJ. This paper makes use of the CASA data reduction package: <http://casa.nrao.edu>—Credit: International consortium of scientists based at the National Radio Astronomical Observatory (NRAO), the European Southern Observatory (ESO), the National Astronomical Observatory of Japan (NAOJ), the CSIRO Australia Telescope National Facility (CSIRO/ATNF), and the Netherlands Institute for Radio Astronomy (ASTRON) under the guidance of NRAO.

Appendix A

Channel Map of the FeO ($\nu = 0$, $\Omega = 4$, $J = 11-10$) Transition at 336.816 GHz

In Figure 6, we present the ALMA channel map of the FeO ($\nu = 0$, $\Omega = 4$, $J = 11 - 10$) emission in R Dor.

Appendix B

Derivation of the Column Density of FeO

($\nu = 0$, $\Omega = 4$, $J = 11$)-state

The brightness temperature, T_b , expresses the observed intensity, I_ν , into the Planck function B_ν :

$$I_\nu = B_\nu(T_b), \quad (3)$$

which in the Rayleigh–Jeans regime simplifies to

$$B_\nu(T_b) = \frac{2k}{\lambda^2} T_b, \quad (4)$$

where k is the Boltzmann constant and λ is the wavelength. The flux density, S_ν^F , of the source is defined as

$$S_\nu^F = \int_S I_\nu(\Omega) d\Omega \quad (5)$$

or

$$S_\nu^F = \frac{2k}{\lambda^2} \int_S T_b(\Omega) d\Omega, \quad (6)$$

Ω here being the solid angle and S denoting that one integrates over the source solid angle $\int_S d\Omega = \Omega_S$. For a source of uniform brightness, $T_b(\Omega)$ can be taken out of the integral and Equation (6) becomes

$$S_\nu^F = \frac{2k}{\lambda^2} T_b \Omega_S. \quad (7)$$

The source size Ω_S is dependent on the observed frequency ν as can be seen in Figure 6. To derive Ω_S for each frequency, we fitted a single 2D Gaussian component to the emission in each channel from the observed frequencies between 336.7006 and 336.7455 GHz. The emission is, however, too compact, patchy, and irregular to deconvolve the beam reliably from the apparent angular size. This was close to the restoring beam ($0''.175 \times 0''.127$) size and showed large uncertainties. We hence assume that the emission is unresolved, and use the beam size ($\Omega_{\text{beam}} = \Omega_S = 0.175 \times 0.127 \times \pi / (4 \ln(2)) = 0.025 \text{ arcsec}^2$) to estimate the brightness temperature.⁹

Defining W as

$$W = \int T_b dv, \quad (8)$$

where v is the velocity (corrected for the v_{LSR}), and using Equation (7) for an integrated flux density of the FeO ($\nu = 0$, $\Omega = 4$, $J = 11-10$) line of $0.79 \text{ Jy km s}^{-1}$, yields $W = 330 \text{ K km s}^{-1}$ (for a source angular size of 150 mas in diameter or $2.5 R_*$ in radius).

Assuming that the emission is optically thin, one can write the column density in the upper state N_u as (Goldsmith & Langer 1999)

$$N_u^{\text{thin}} = \frac{8\pi k \nu^2 W}{hc^3 A_{i,j}}, \quad (9)$$

where k is the Boltzmann constant, c is the velocity of light, and $A_{i,j}$ is the Einstein-A coefficient for the transition. For a linear molecule, the Einstein-A coefficient for a rotational transition $J \rightarrow J - 1$ is given by (Tielens 2010)

$$A_{i,j} = \frac{64\pi^4 \nu^3 \mu_{i,j}^2}{3hc^3}, \quad (10)$$

where $\mu_{i,j}$ is the transition moment and h is the Planck constant. For a transition $J \rightarrow J - 1$, the transition moment

⁹ If one used the moment-0 maps to derive the source size, one would obtain a larger angular size of $\sim 0''.360$, as the emission is slightly offset from channel to channel, which makes the moment-0 image slightly enlarged. The brightness temperature derived from Equation (7) would be a factor 5.7 lower when using this larger source angular size.

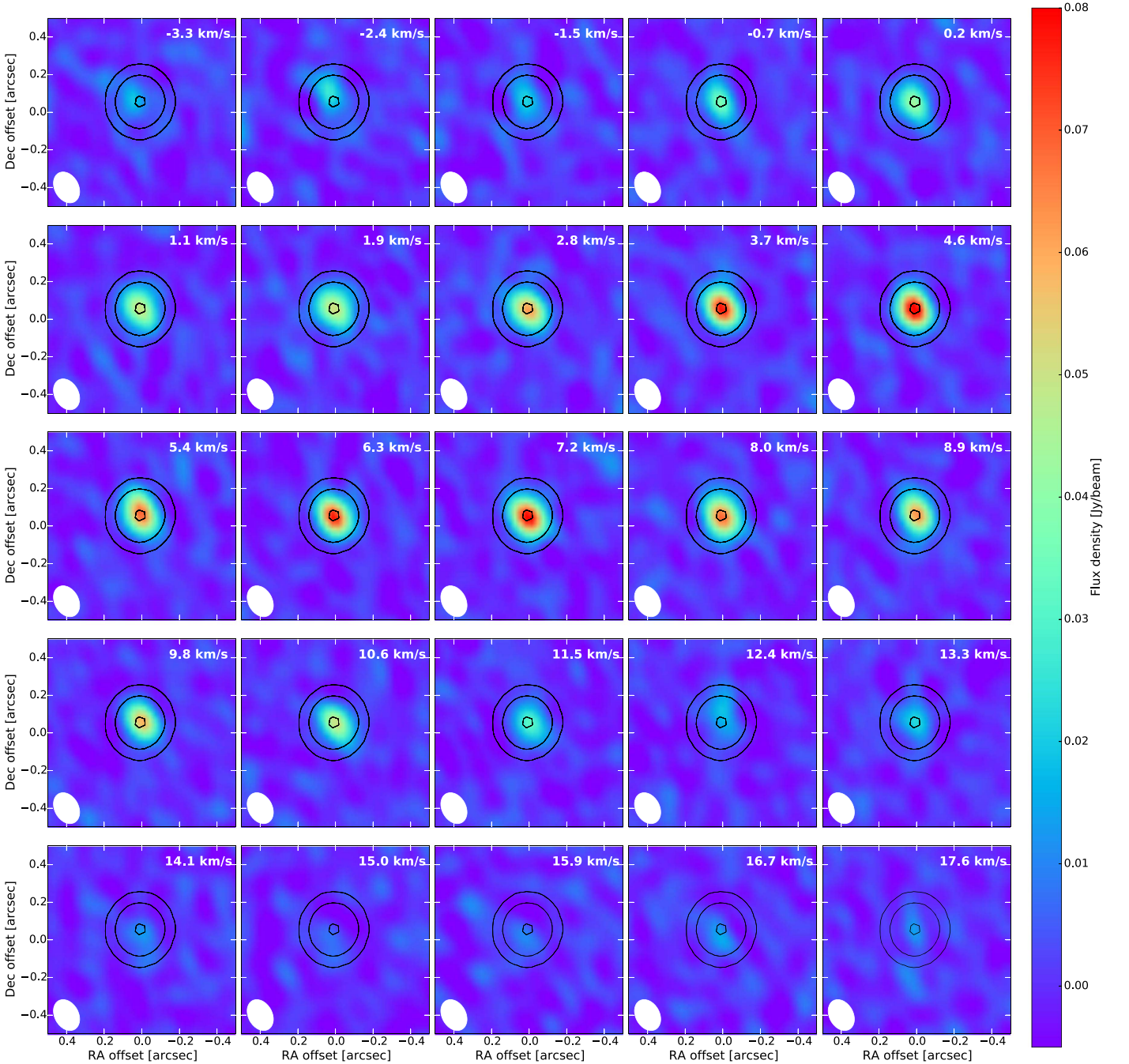


Figure 6. Channel map of the FeO ($\nu = 0$, $\Omega = 4$, $J = 11-10$) emission in R Dor. The circle denotes the place of maximum dust emissivity (taking the contours at 1%, 10%, and 90% of the total flux). The local standard of rest velocity, v_{LSR} , of R Dor is $\sim 7 \text{ km s}^{-1}$ (Decin et al. 2018). The TiO₂ ($23_{8,16}-23_{7,17}$) transition at 266.8241 GHz slightly blends the FeO line in the blue wing.

$$\mu_{i,j}^2 = \mu^2 \frac{S}{2J+1} \quad (11)$$

and the quantum-mechanical line strength S is calculated with the standard expression for a symmetric top by replacing K , the angular momentum along the symmetry axis of the symmetric top, by Ω the projection of the angular momentum along the molecular axis (Merer et al. 1982)

$$\mu_{J,J-1}^2 = \mu^2 \frac{J^2 - \Omega^2}{J(2J+1)}, \quad (12)$$

where μ is the permanent electric dipole moment. This yields

$$A_{J,J-1} = 1.16 \times 10^{-11} \mu^2 \nu^3 \frac{J^2 - \Omega^2}{J(2J+1)} \quad (13)$$

for ν in GHz and μ in Debye. Hence,

$$N_u^{\text{thin}} = \frac{1.64 \times 10^{14}}{\nu \mu^2} \frac{J(2J+1)}{J^2 - \Omega^2} W, \quad (14)$$

for W in units of Jy km s^{-1} . Using a permanent electric dipole moment of 4.7 Debye (Steimle et al. 1989), we obtain that $N_u^{\text{thin}} = 1.7 \times 10^{13} \text{ cm}^{-2}$.

Table 2Rotational Transitions in the FeO ($\nu = 0, \Omega = 4$) Ladder Calculated with the Spectroscopic Constants of Allen et al. (1996)

Frequency (MHz)	E_{up} (cm^{-1})	$J \rightarrow J - 1$	$A_{J,J-1}$ (s^{-1})
153135.0938	5.1080	5 \rightarrow 4	1.5058e-04
183757.0156	11.2375	6 \rightarrow 5	4.0768e-04
214376.1719	18.3883	7 \rightarrow 6	7.9343e-04
244992.0938	26.5604	8 \rightarrow 7	1.3299e-03
275604.3125	35.7535	9 \rightarrow 8	2.0391e-03
306212.4062	45.9677	10 \rightarrow 9	2.9429e-03
336815.8750	57.2027	11 \rightarrow 10	4.0635e-03
367414.2500	69.4583	12 \rightarrow 11	5.4226e-03
398007.1250	82.7344	13 \rightarrow 12	7.0422e-03
428594.0312	97.0307	14 \rightarrow 13	8.9441e-03
459174.5000	112.3471	15 \rightarrow 14	1.1150e-02
489748.0938	128.6834	16 \rightarrow 15	1.3682e-02
520314.3750	146.0392	17 \rightarrow 16	1.6561e-02
550872.8750	164.4143	18 \rightarrow 17	1.9810e-02
581423.1250	183.8085	19 \rightarrow 18	2.3449e-02
611964.7500	204.2215	20 \rightarrow 19	2.7501e-02
642497.2500	225.6529	21 \rightarrow 20	3.1987e-02
673020.2500	248.1024	22 \rightarrow 21	3.6927e-02
703533.2500	271.5698	23 \rightarrow 22	4.2345e-02
734035.8125	296.0546	24 \rightarrow 23	4.8260e-02
764527.5625	321.5565	25 \rightarrow 24	5.4694e-02
795008.0625	348.0751	26 \rightarrow 25	6.1668e-02
825476.8750	375.6100	27 \rightarrow 26	6.9204e-02
855933.6250	404.1609	28 \rightarrow 27	7.7322e-02
886377.7500	433.7273	29 \rightarrow 28	8.6043e-02
916809.0000	464.3087	30 \rightarrow 29	9.5387e-02
947226.8750	495.9048	31 \rightarrow 30	1.0538e-01
977631.0625	528.5151	32 \rightarrow 31	1.1603e-01
1008021.0000	562.1390	33 \rightarrow 32	1.2737e-01
1038396.4375	596.7762	34 \rightarrow 33	1.3942e-01
1068756.8750	632.4261	35 \rightarrow 34	1.5219e-01
1099102.0000	669.0882	36 \rightarrow 35	1.6571e-01
1129431.5000	706.7620	37 \rightarrow 36	1.8000e-01
1159744.7500	745.4469	38 \rightarrow 37	1.9507e-01
1190041.6250	785.1424	39 \rightarrow 38	2.1095e-01
1220321.6250	825.8480	40 \rightarrow 39	2.2766e-01
1250584.3750	867.5630	41 \rightarrow 40	2.4521e-01
1280829.5000	910.2868	42 \rightarrow 41	2.6363e-01
1311056.7500	954.0190	43 \rightarrow 42	2.8294e-01
1341265.6250	998.7588	44 \rightarrow 43	3.0315e-01

Note. Listed are the rotational frequency, upper state energy, rotational quantum numbers, and Einstein-A coefficient.

Appendix C

Rotational Transition Frequencies, Upper State Energies, and Einstein-A Coefficients in the FeO ($\nu = 0, \Omega = 4$)-state

We calculated the rotational transition frequencies and upper state energies, E_{up} , in the FeO ($\nu = 0, \Omega = 4$) spin component by using the leading spectroscopic constants in Allen et al. (1996) and following Merer et al. (1982). The Einstein-A coefficients are calculated from Equation (13); see Table 2. By comparison with the results of Allen et al. (1996), who measured the FeO spectrum for frequencies lower than 400 GHz, the accuracy of the calculated frequencies is about 1 MHz. This is sufficient for our radiative transfer calculations, but we note that for spectroscopic identifications the required accuracy of the calculated frequencies in Table 2 should be higher.

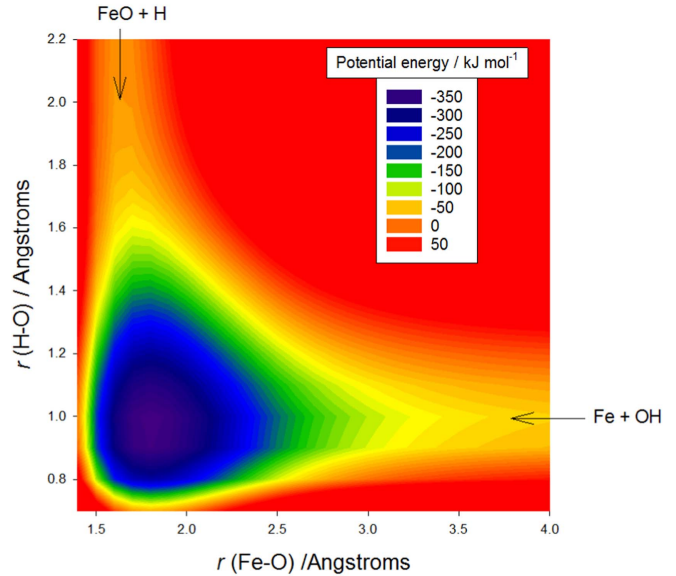


Figure 7. Diagram of the potential energy surface for the Fe+OH \rightarrow FeO+H reaction (R42), calculated for a fixed Fe–O–H angle of 150° at the b3lyp/6-311 + g(2d,p) level of theory using the GAUSSIAN 16 suite of programs (Frisch et al. 2016). Note the absence of barriers in the entrance channels for R42 (Fe+OH) or R43 (FeO+H). The deep well in the surface is due to the formation of FeOH.

Appendix D

Reactions Used in the Chemical Kinetics Code

The gas-phase chemical network used in this study contains seven atomic (H, He, C, O, Ca, Mg, and Fe) and 15 molecular (H_2 , H_2O , O_2 , OH, CO, CO_2 , CaO, CaOH, CaH, MgO, MgOH, MgH, FeO, FeOH, and FeH) species that take part in 59 reactions. The gas-phase reaction rate coefficients are taken from the literature where available, and extrapolated to the high temperatures of an outflow using TST (Atkins 1998), with molecular constants (vibrational frequencies, rotational constants) calculated using quantum theory. The rate coefficients for reverse reactions were then calculated assuming detailed balance.

Most of the uncertainty in the TST calculations arises from the accuracy of the energy barrier. For most of this work, we have calculated the equilibrium constant and then used this for detailed balance where either the forward or backward reaction has been measured (i.e., barrier not needed). In some cases, a TST expression is fitted to a measured rate constant, with the barrier calculated from quantum theory adjusted to optimize the fit. This greatly improves the accuracy of the estimated rate constants. An example of our applied methodology and resulting accuracy can, e.g., be found in Self & Plane (2003) for reactions R38 and R39.

A special note concerns reactions R42 and R43; we have calculated the potential energy surface for these reactions. Figure 7 illustrates the surface for a fixed Fe–O–H angle of 150° . Note there are no barriers in the entry channels of either R42 (Fe+OH) or R43 (FeO+H). We have therefore set the barrier of R43 to zero in the expression estimated by Rumminger et al. (1999). R42 is endothermic by $25.5 \pm 5.8 \text{ kJ mol}^{-1}$, using the measured FeO bond energy (0 K) of $398.5 \pm 5.8 \text{ kJ mol}^{-1}$ (Metz et al. 2005). The rate coefficient for R42 can then be calculated by detailed balance, yielding $k_{42}(T)$.

Table 3
Reaction Rates for the Gas-phase Chemical Processes Used in This Study^a

Number	Reactants		Products	A	n	E_a	Reference and Comments ^b
R1	H+H+H ₂	→	H ₂ +H ₂	8.85e-33	-0.60	0.0	NIST
R3	H+H+H	→	H ₂ +H	8.82e-33	0.00	0.0	NIST
R5	H+H+He	→	H ₂ +He	4.96e-33	0.00	0.0	NIST
R7	OH+OH	→	H ₂ O+O	1.65e-12	1.10	50.5	NIST
R8	O+H ₂ O	→	OH+OH	1.84e-11	0.95	8573.7	NIST
R9	OH+CO	→	CO ₂ +H	3.52e-12	0.00	2630.2	NIST
R10	H+CO ₂	→	OH+CO	2.51e-10	0.00	13229.1	NIST
R11	OH+H ₂ O+H	→	H ₂ O+H ₂ O	1.19e-30	-2.10	0.0	NIST
R13	OH+H	→	H ₂ +O	6.86e-14	2.80	1949.5	NIST
R14	O+H ₂	→	OH+H	3.44e-13	2.67	3159.3	NIST
R15	H ₂ +OH	→	H ₂ O+H	1.55e-12	1.60	1659.7	NIST
R16	H+H ₂ O	→	H ₂ +OH	6.82e-12	1.60	9719.8	NIST
R17	C+O	→	CO	1.58e-17	0.34	1297.4	Dalgarno et al. (1990)
R18	C+O+M	→	CO+M	2.00e-34	0.00	0.0	NIST
R19	CO+O+M	→	CO ₂ +M	1.20e-32	0.00	2160.0	NIST
R20	H+O+M	→	OH+M	4.36e-32	-1.00	0.0	NIST
R21	OH+H+M	→	H ₂ O+M	2.59e-31	-2.00	0.0	NIST
R26	Ca+H ₂ O	→	CaO+H ₂	1.70e-09	0.00	8749.0	TST estimate
R27	CaO+H ₂	→	Ca+H ₂ O	3.40e-10	0.00	0.0	Broadley & Plane (2010)
R28	Ca+H ₂ O	→	CaOH+H	1.90e-09	0.00	19110.0	TST estimate
R29	CaOH+H	→	Ca+H ₂ O	1.00e-10	0.00	0.0	Gomez-Martin & Plane (2017)
R30	Ca+OH	→	CaO+H	3.60e-10	0.00	4785.0	TST estimate
R31	CaO+H	→	Ca+OH	1.70e-10	0.00	3020.0	estimated as R43
R32	CaO+H ₂	→	CaOH+H	2.92e-12	0.00	-2050.0	Cotton & Jenkins (1971)
R33	CaOH+H	→	CaO+H ₂	4.48e-12	0.00	0.0	NIST
R34	Ca+CO ₂	→	CaO+CO	3.20e-09	0.00	14907.0	TST estimate
R35	CaO+CO	→	Ca+CO ₂	1.10e-11	0.00	0.0	estimated as R55
R36	Ca+O ₂	→	CaO+O	7.30e-09	0.00	11028.0	TST estimate
R37	CaO+O	→	Ca+O ₂	1.10e-09	0.00	421.0	Broadley & Plane (2010)
R38	Fe+O ₂	→	FeO+O	2.09e-10	0.00	10200.0	NIST
R39	FeO+O	→	Fe+O ₂	4.60e-10	0.00	350.0	Self & Plane (2003)
R40	Fe+H ₂ O	→	FeO+H ₂	8.80e-11	0.00	11925.0	TST estimate
R41	FeO+H ₂	→	Fe+H ₂ O	2.60e-11	0.00	5384.0	TST estimate
R42	Fe+OH	→	FeO+H	2.40e-10	0.00	3348.0	detailed balance
R43	FeO+H	→	Fe+OH	1.70e-10	0.00	0.00	Rumminger et al. (1999)
R44	Fe+CO ₂	→	FeO+CO	2.00e-09	0.00	16670.0	TST estimate
R45	FeO+CO	→	Fe+CO ₂	1.20e-13	2.31	820.0	TST estimate
R46	Fe+Fe+M	→	Fe ₂ +M	1.12e-31	-0.52	7454.0	NIST
R48	Mg+H ₂ O	→	MgO+H ₂	5.80e-10	0.00	29435.0	TST estimate
R49	MgO+H ₂	→	Mg+H ₂ O	1.20e-10	0.00	1700.0	TST estimate
R50	Mg+H ₂ O	→	MgOH+H	1.10e-08	0.00	23173.0	TST estimate
R51	MgOH+H	→	Mg+H ₂ O	1.00e-10	0.00	0.0	estimated as R29
R52	Mg+OH	→	MgO+H	3.40e-10	0.00	23651.0	TST estimate
R53	MgO+H	→	Mg+OH	1.70e-10	0.00	3020.0	estimated as R43
R54	Mg+CO ₂	→	MgO+CO	3.00e-09	0.00	33054.0	TST estimate
R55	MgO+CO	→	Mg+CO ₂	1.10e-11	0.00	0.0	TST estimate
R56	Mg+O ₂	→	MgO+O	3.00e-09	0.00	26584.0	TST estimate
R57	MgO+O	→	Mg+O ₂	6.20e-10	0.00	0.0	Plane et al. (2012)
R58	Fe+H ₂ O	→	FeOH+H	1.90e-10	0.00	18685.0	TST estimate
R59	FeOH+H	→	Fe+H ₂ O	1.00e-10	0.00	0.0	estimated as R29

Notes.

^a The rates are given in the Arrhenius form $k(T) = A \times \left(\frac{T}{300}\right)^n \times \exp(-E_a/T)$, where T is the gas temperature, A is the Arrhenius coefficient in $\text{cm}^3 \text{s}^{-1}$ or $\text{cm}^6 \text{s}^{-1}$ for a bimolecular or termolecular process, respectively, n is the temperature dependence of the rate coefficient, and E_a is the activation energy barrier in K.

^b NIST: National Institute for Standards and Technology (<http://kinetics.nist.gov>), TST estimate: estimation of the rate by transition state theory.

The list of all chemical reactions involved is given in Table 3.

J. M. C. Plane  <https://orcid.org/0000-0003-3648-6893>

C. A. Gottlieb  <https://orcid.org/0000-0003-2845-5317>

ORCID iDs

L. Decin  <https://orcid.org/0000-0002-5342-8612>

D. Gobrecht  <https://orcid.org/0000-0002-3443-3416>

References

- Allen, M. D., Ziurys, L. M., & Brown, J. M. 1996, *CPL*, 257, 130
 Atkins, P. W. 1998, *Physical Chemistry* (6th ed.; Oxford: Oxford Univ. Press)
 Bedding, T. R., Zijlstra, A. A., Jones, A., & Foster, G. 1998, *MNRAS*, 301, 1073

- Bertschinger, E., & Chevalier, R. A. 1985, *ApJ*, **299**, 167
- Broadley, S. L., & Plane, J. M. C. 2010, *PCCP*, **12**, 9094
- Castelaz, M. W., Luttermoser, D. G., Caton, D. B., & Piontek, R. A. 2000, *AJ*, **120**, 2627
- Cherchneff, I. 2006, *A&A*, **456**, 1001
- Cheung, A. S.-C., Gordon, R. M., & Merer, A. J. 1981, *JMoSp*, **87**, 289
- Cheung, A. S.-C., Lee, N., Lyyra, A. M., Merer, A. J., & Taylor, A. W. 1982, *JMoSp*, **95**, 213
- Cotton, D. H., & Jenkins, D. R. 1971, *Trans. Faraday Soc.*, **67**, 730
- Cristallo, S., Straniero, O., Piersanti, L., & Gobrecht, D. 2015, *ApJS*, **219**, 40
- Dalgarno, A., Du, M. L., & You, J. H. 1990, *ApJ*, **349**, 675
- Dayou, F., & Balança, C. 2006, *A&A*, **459**, 297
- De Beck, E., Decin, L., Ramstedt, S., et al. 2017, *A&A*, **598**, A53
- De Beck, E., Vlemmings, W., Muller, S., et al. 2015, *A&A*, **580**, A36
- Decin, L., De Beck, E., Brünken, S., et al. 2010, *A&A*, **516**, A69
- Decin, L., Richards, A. M. S., Danilovich, T., Homan, W., & Nuth, J. A. 2018, *A&A*, in press
- Decin, L., Richards, A. M. S., Waters, L. B. F. M., et al. 2017, *A&A*, **608**, A55
- Elitzur, M., Goldreich, P., & Scoville, N. 1976, *ApJ*, **205**, 384
- Endres, C. P., Schlemmer, S., Schilke, P., Stutzki, J., & Müller, H. S. P. 2016, *JMoSp*, **327**, 95
- Freytag, B., Liljegren, S., & Höfner, S. 2017, *A&A*, **600**, A137
- Frisch, M. J., Trucks, G. W., Schlegel, H. B., et al. 2016, Gaussian16 Revision A.03 (Wallingford, CT: Gaussian Inc.), <http://gaussian.com/gaussian16/>
- Furuya, R. S., Walmsley, C. M., Nakanishi, K., Schilke, P., & Bachiller, R. 2003, *A&A*, **409**, L21
- Gail, H.-P., & Sedlmayr, E. 2013, *Physics and Chemistry of Circumstellar Dust Shells* (Cambridge: Cambridge Univ. Press)
- Gobrecht, D., Cherchneff, I., Sarangi, A., Plane, J. M. C., & Bromley, S. T. 2016, *A&A*, **585**, A6
- Goldsmith, P. F., & Langer, W. D. 1999, *ApJ*, **517**, 209
- Gomez-Martin, J. C., & Plane, J. M. C. 2017, *Earth Space Chem.*, **1**, 431
- Green, S., & Thaddeus, P. 1974, *ApJ*, **191**, 653
- Hirano, T., Nagashima, U., Winnewisser, G., & Jensen, P. 2010, *JChPh*, **132**, 094303
- Hocking, W. H., Winnewisser, G., Churchwell, E., & Percival, J. 1979, *A&A*, **75**, 268
- Kamiński, T., Gottlieb, C. A., Young, K. H., Menten, K. M., & Patel, N. A. 2013, *ApJS*, **209**, 38
- Kamiński, T., Müller, H. S. P., Schmidt, M. R., et al. 2017, *A&A*, **599**, A59
- Kamiński, T., Wong, K. T., Schmidt, M. R., et al. 2016, *A&A*, **592**, A42
- Khouri, T., Maercker, M., Waters, L. B. F. M., et al. 2016, *A&A*, **591**, A70
- Maercker, M., Schöier, F. L., Olofsson, H., Bergman, P., & Ramstedt, S. 2008, *A&A*, **479**, 779
- McMullin, J. P., Waters, B., Schiebel, D., Young, W., & Golap, K. 2007, in *ASP Conf. Ser. 376, Astronomical Data Analysis Software and Systems XVI*, ed. R. A. Shaw, F. Hill, & D. J. Bell (San Francisco, CA: ASP), 127
- Merer, A. J., Walmsley, C. M., & Churchwell, E. 1982, *ApJ*, **256**, 151
- Metz, R. B., Nicolas, C., Ahmed, M., & Leone, S. R. 2005, *JChPh*, **123**, 114313
- Müller, H. S. P., Schlöder, F., Stutzki, J., & Winnewisser, G. 2005, *JMoSt*, **742**, 215
- Müller, H. S. P., Thorwirth, S., Roth, D. A., & Winnewisser, G. 2001, *A&A*, **370**, L49
- Nowotny, W., Höfner, S., & Aringer, B. 2010, *A&A*, **514**, A35
- Pickett, H. M., Poynter, R. L., Cohen, E. A., et al. 1998, *JQSRT*, **60**, 883
- Plane, J. M. C., Whalley, C. L., Frances-Soriano, L., et al. 2012, *JChPh*, **137**, 014310
- Quintana-Lacaci, G., Agúndez, M., Cernicharo, J., et al. 2016, *A&A*, **592**, A51
- Rumminger, M. D., Reinelt, D., Babushock, V., & Linteris, G. T. 1999, *CoFI*, **116**, 207
- Sánchez Contreras, C., Velilla Prieto, L., Agúndez, M., et al. 2015, *A&A*, **577**, A52
- Scalo, J. M., & Ross, J. E. 1976, *A&A*, **48**, 219
- Schöier, F. L., Olofsson, H., Wong, T., Lindqvist, M., & Kerschbaum, F. 2004, *A&A*, **422**, 651
- Schöier, F. L., van der Tak, F. F. S., van Dishoeck, E. F., & Black, J. H. 2005, *A&A*, **432**, 369
- Self, D. E., & Plane, J. M. C. 2003, *PCCP*, **5**, 1407
- Steimle, T. C., Nachman, D. F., Shirley, J. E., & Merer, A. J. 1989, *JChPh*, **90**, 5360
- Thaddeus, P., Cummins, S. E., & Linke, R. A. 1984, *ApJL*, **283**, L45
- Tielens, A. G. G. M. 2010, *The Physics and Chemistry of the Interstellar Medium* (Cambridge: Cambridge Univ. Press)
- Velilla Prieto, L., Sánchez Contreras, C., Cernicharo, J., et al. 2017, *A&A*, **597**, A25
- Walmsley, C. M., Bachiller, R., Pineau des Forêts, G., & Schilke, P. 2002, *ApJL*, **566**, L109